npj | climate and atmospheric science

www.nature.com/npjclimatsci

ARTICLE OPEN

Check for updates

A comprehensive dataset of luminescence chronologies and environmental proxy indices of loess-paleosol deposits across Asia

Guoqiang Li[1]✉, Zhongfeng Yan[1], Yougui Song[2]✉, Kathryn E. Fitzsimmons[3]✉, Shuangwen Yi[4]✉, Shugang Kang[2]✉, Chongyi E[5]✉, Thomas Stevens[6,7]✉, Zhongping Lai[8]✉, Aditi K. Dave[3,9]✉, Chunzhu Chen[10]✉, Yanqing Deng[1]✉, He Yang[11]✉, Leibin Wang[12], Xiaojian Zhang[4], Caixin Qin[1], Qiuyue Zhao[13], Jan-Pieter Buylaert[14], Tao Lu[15], Yixuan Wang[15], Xiangjun Liu[16], Zhiyong Ling[15], Qiufang Chang[17], Haitao Wei[1], Xiaoyan Wang[1] and Fahu Chen[18]✉

Loess-paleosol sequences have been used in Asia to study climate and environmental changes during the Quaternary. The scarcity of age control datasets and proxy indices analysis data for Asian loess has limited our understanding of loess depositional processes and the reconstruction of paleoclimatic changes from loess-paleosol records. In this study, we present a dataset that includes 1785 quartz optically stimulated luminescence ages and 1038 K-feldspar post-infrared infrared stimulated luminescence ages from 128 loess-paleosol sequences located in different regions of Asia. We generate 38 high-resolution age-depth models of loess records based on the provided datasets. We provide data on 12,365 grain size records, 14,964 magnetic susceptibility records, 2204 $CaCO_3$ content records, and 3326 color reflection records. This dataset contains the most detailed and accurate chronologies and proxy index data for loess records in Asia yet published. It provides fundamental data for understanding the spatial-temporal variations in loess depositional processes and climatic changes across the continent during the mid-late Quaternary.

npj Climate and Atmospheric Science (2024)7:7 ; https://doi.org/10.1038/s41612-023-00555-4

INTRODUCTION

Eolian loess is a wind-blown silt-dominated sediment mostly formed during the Quaternary period, which covers ~10% of the land surface of the planet[1,2]. Generally, it has a homogenous and porous structure and consists primarily of quartz and feldspar grains[3]. Loess in Asia is mainly distributed across arid and semi-arid regions of mid-latitude Central and East Asia, with some sporadic distribution in Western Asia[4]. These regions include the northern Iranian loess plateau[5], piedmont regions of the high mountains in Central Asia and NW China[2], Chinese Central Loess Plateau[6], NE China[7], the Tibetan Plateau[8] and some coastal regions of the Shandong Peninsula[9], and southwestern and northeastern Siberia[10]. Loess-paleosol sequences from the Chinese Central Loess Plateau have long been regarded as globally important archives for paleoclimatic and environmental changes due to their relatively continuous and high dust deposition rates on both orbital and suborbital timescales, thus consequently acting as sensitive archives of the interplay of the East Asian summer and winter monsoon (EASM and EAWM, respectively)[6,11–14]. Similarly, loess-paleosol sequences across different regions of Asia have great potential for unraveling the Quaternary climatic and environmental changes in regions of Asia where the interaction of westerlies, the Asian monsoon systems, and high altitude air masses influence the climate over different timescales[15–17]. However, loess-paleosol records from different regions beyond the Chinese Central Loess Plateau are still poorly understood, primarily due to the limited availability of independent age control and proxy indices for paleoclimatic reconstruction.

Although radiocarbon dating is widely used in terrestrial settings, this method of is problematic for dating loess deposits from arid and/or semi-arid regions of mid-latitude Asia because of the general lack of reliable dating materials (e.g., plant remains and charcoal)[18] and the upper age limits of c. 40 kyr BP which prevent chronological constraints of the lower parts of long loess records. Furthermore, the use of carbonate and bulk organic matter of loess-paleosol sequence may cause overestimation related to redeposition of older carbon[19,20] or underestimation

[1]Key Laboratory of Western China's Environmental Systems (Ministry of Education), College of Earth and Environmental Sciences, Lanzhou University, Lanzhou 730000, China. [2]State Key Laboratory of Loess and Quaternary Geology, Institute of Earth Environment, Chinese Academy of Sciences, Xi'an, China. [3]Department of Geosciences, University of Tübingen, Schnarrenbergstrasse 94-96, 72076 Tübingen, Germany. [4]School of Geography and Ocean Science, Nanjing University, Nanjing 210023, China. [5]Qinghai Provincial Key Laboratory of Physical Geography and Environmental Processes, School of Geographical Science, Qinghai Normal University, Xining 810008, China. [6]Department of Earth Sciences, Uppsala University, Villavagen 16, Uppsala 75236, Sweden. [7]Department of Geosciences and Geography, University of Helsinki, P.O. Box 64, 00014 Helsinki, Finland. [8]Institute of Marine Sciences, Guangdong Provincial Key Laboratory of Marine Disaster Prediction and Protection, Shantou University, Shantou, Guangdong 515063, China. [9]Interdisciplinary Research Institute on Bionanosciences, Babes Bolyai University, Cluj-Napoca, Romania. [10]School of Geographic Science, Nantong University, Nantong 226007, China. [11]School of Atmospheric Sciences, Chengdu University of Information Technology, Chengdu 610000, China. [12]Centre for Climate and Environmental Changes, School of Geographical Sciences, Guangzhou University, Guangzhou, Guangdong 510006, China. [13]Key Laboratory of Tourism and Resources Environment in Universities of Shandong, Taishan University, 271000 Taian, China. [14]Department of Physics, Technical University of Denmark, DTU Risø Campus, Roskilde, Denmark. [15]Key Laboratory of Salt Lake Geology and Environment of Qinghai Province, Qinghai Institute of Salt Lakes, Chinese Academy of Sciences, Xining 810008, China. [16]School of Geography and Tourism, Jiaying University, Meizhou, China. [17]School of Geography and Tourism, Zhengzhou Normal University, Zhengzhou, China. [18]Key Laboratory of Alpine Ecology (LAE), CAS Center for Excellence in Tibetan Plateau Earth Sciences, Institute of Tibetan Plateau Research, Chinese Academy of Sciences (CAS), Beijing 100101, China. ✉email: gqli@lzu.edu.cn; ygsong@loess.llqg.ac.cn; kathryn.fitzsimmons@uni-tuebingen.de; ysw7563@nju.edu.cn; kshg@ieecas.cn; echongyi@163.com; thomas.stevens@geo.uu.se; zhongping_lai@stu.edu.cn; aditikrishna.dave@gmail.com; pollenchencz@gmail.com; dengyq19@lzu.edu.cn; yanghe@cuit.edu.cn; fhchen@itpcas.ac.cn

related to younger materials incorporation through bioturbation, penetration, and subsequent decomposition of rootlets or translocation of soluble organic matter[21,22].

Luminescence dating techniques, which include the widely used optically stimulated luminescence (OSL) and infrared stimulated luminescence (IRSL), determine the ages of eolian deposits by directly measuring last exposure of quartz or feldspar minerals to light, and thereby the depositional process[23]. Quartz OSL dating is now widely applied to the dating of late Quaternary sediments[24], and has been successfully used to establish the chronology of loess records from different regions of Asia[2,5,8–10,16,17,25–28]. Owing to the luminescence signal saturation characteristics of the quartz mineral, it has been observed that quartz OSL dating can be used to reliably date loess samples up to 50–60 ka from the Chinese Central Loess Plateau and up to 40–70 ka for samples from Tibetan Plateau and Central Asia[16,17,29–33]. The more recently developed approach of K-feldspar post-InfraRed InfraRed (pIRIR) dating, using a post-IR IRSL signal, can be used to date loess samples up to 250–300 ka[34–36] and has been successfully applied to loess-paleosol sequences in different regions of Asia[7,16,17,25,30,37,38]. High-resolution luminescence dating of loess-paleosol sequences from the Tianshan Mountain piedmont, Tibetan Plateau, northern Iran loess plateau and Chinese Central Loess Plateau shows that depositional hiatuses spanning a few ka to as much as 60 ka occurred in loess-paleosol sequences in these regions[5,16,25,30,32,39], suggesting that high-resolution absolute chronological information is necessary for the reconstruction and interpretation of paleoclimatic changes from loess records. Furthermore, proxy index analyses of loess records from different regions of arid mid-latitude Central Asia are still limited, especially the data spanning the past glacial-interglacial cycle. As yet, there is no publicly available dataset covering systematic quartz and K-feldspar luminescence chronologies and proxy index analyses from loess-paleosol sequences from different regions of Asia. Indeed, data scarcity has significantly hindered our understanding of loess depositional processes and reconstruction of paleoclimatic changes from loess-paleosol records in different regions of Asia.

In this study, we compile a comprehensive dataset of quartz OSL and K-feldspar pIRIR ages, and construct high-resolution age-depth models from loess records in Asia spanning the past 250–300 ka, based on these ages. Furthermore, we also collate proxy index datasets of grain size, magnetic susceptibility, $CaCO_3$ content and color reflection for loess records across different regions of Asia (Supplementary Fig. 1). This dataset comprises 1785 quartz and 1038 K-feldspar pIRIR ages from 128 loess-paleosol sequences and 38 high-resolution age-depth models of loess records, and a total of 12,365 granulometric records including mean grain size, clay fraction (e.g., <2 μm, %), silt fraction (e.g., 2–63 μm, %) and sand fraction (>63 μm, %), 14,964 magnetic susceptibility records, 2204 $CaCO_3$ content records and 3326 color reflections records from loess-paleosol sequences from Asia. This dataset can provide the fundamental basis for analyzing the characteristics of loess and paleosols in different geographical regions of Asia, and clarifying spatio-temporal changes in loess depositional processes and loess mass accumulation rate across Asia during mid to -late Quaternary. This dataset can also be used for late Quaternary climatic reconstruction for mid-latitude Asia, as well as for comparison with climatic reconstructions from neighboring European loess records[40]. In addition, the dataset also facilitates evaluation and understanding of how dust emission and loess depositional processes respond to the influence of and/or the interaction with different climatic systems of westerlies, EASM and EAWM over varying timescales.

RESULTS

Luminescence chronologies and proxy indices of Asian loess

A total of 128 loess-paleosol sections across different regions of Asia were investigated and sampled (Supplementary Fig. 2), including 5 sections with depths of 1.24–50.00 m from northern Iranian loess Plateau, 32 sections with depths of 1.4–44.0 m from Central Asia, 52 sections with depths of 0.48–36.20 m from the Tibetan Plateau, 20 sections with depths of 2.85–36.00 m from Chinese Central Loess Plateau, 13 sections from the Shandong Peninsula of eastern China, 4 sections from NE China, and 2 sections from western Siberia, respectively. Detailed information and references of these sections can be found in the Supplementary Table 1. The data corresponding to 2823 luminescence ages including 1785 quartz OSL and 1038 K-feldspar pIRIR ages were collected from published records of the aforementioned 128 loess-paleosol sequences across different regions of Asia. The age-depth modeling of 38 loess-paleosol sections, spanning the past 250–300 ka, was reconstructed based on close-spaced quartz OSL ages and/ or K-feldspar pIRIR ages from each section. As far as we know, this dataset includes the most detailed and accurate previously published record of quartz OSL and K-feldspar pIRIR ages, as well as a number of age-depth models based on luminescence ages for eolian records across Asia.

A total of 12,365 grain size, 14,964 magnetic susceptibility, 2204 $CaCO_3$ content and 3326 color reflection data was collected for samples from these loess-paleosol sequences. It must be noted that 51 of the 128 sections compiled this paper does not have any data on proxy indices, and hence, this should be kept in mind while reconstructing large-scale palaeoclimatic variations over Asia. The detailed location and depth information of each section is listed in Supplementary Table 1, and illustrated here in Fig. 1.

These loess-paleosol sections compiled here, not only cover a large geographical extent but also different geomorphological and elevation settings, and spans different climatic systems of westerlies, EASM, EAWM, and ISM[2,6,11,26]. Thus, the ~250 ka dataset of absolute chronology and proxy indices of these loess-paleosol sequences, makes this the most comprehensive and representative dataset to date for mid to late Quaternary loess deposition and paleoclimatic reconstruction across mid-latitude Asia. The dataset presented in this article is freely available through the National Tibetan Plateau/Third Pole Environment Data Center, https://doi.org/10.11888/Paleoenv.tpdc.300496[41].

DISCUSSION

The concentration of U in loess samples from Asia generally varies between 1 and 4 ppm, except a few samples that either have very low values of 0.5–1.0 ppm or very high values of 4–5 ppm. The average U concentration of loess samples from all over Asia is 2.53 ± 0.01 ppm ($n = 2246$), while the regional average U concentration of loess samples from Western Asia, Central Asia, Tibetan Plateau, Chinese Central Loess plateau, NE China, Shandong Peninsula and Western Siberia is 2.44 ± 0.04 ppm ($n = 104$), 2.93 ± 0.03 ppm ($n = 528$), 2.41 ± 0.03 ppm ($n = 537$), 2.57 ± 0.02 ppm ($n = 716$), 1.93 ± 0.04 ppm ($n = 66$), 1.98 ± 0.03 ppm ($n = 237$) and 2.73 ± 0.12 ppm ($n = 58$), respectively (Fig. 2a). The concentration of Th in loess samples from Asia varies between 6 and 16 ppm, wherein a few samples either have comparatively slightly higher or lower values of 16–37 and 2–6 ppm, respectively. The average Th concentration of loess samples across mid-latitude Asia is 11.21 ± 0.05 ppm ($n = 2398$), while the regional average Th concentration of loess samples from Western Asia, Central Asia, Tibetan Plateau, Chinese Central Loess Plateau, NE China, Shandong Peninsula and Western Siberia is 9.44 ± 0.15 ppm ($n = 104$), 11.54 ± 0.09 ppm ($n = 528$), 11.45 ± 0.13 ppm ($n = 537$), 11.32 ± 0.06 ppm ($n = 868$), 8.49 ± 0.20 ppm ($n = 66$), 11.25 ± 0.13 ppm ($n = 237$) and 10.42 ± 0.17 ppm ($n = 58$), respectively (Fig. 2b). The K content of

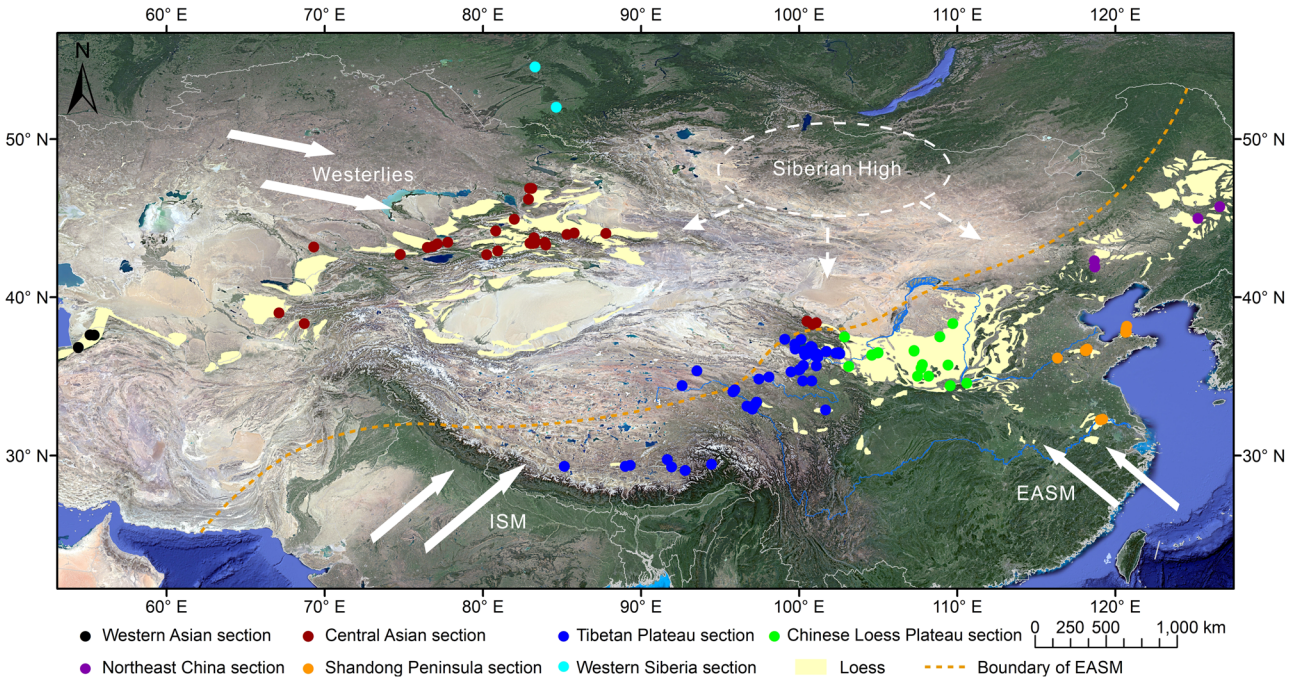

Fig. 1 The map of loess distribution and locations of loess-paleosol sections in the different regions of Asia. The software 91 satellite map (https://www.91weitu.com/) was used to download the satellite imagery from Google Earth. The map generation was performed in software ArcGIS 10.7.

loess samples from Asia varies between 0.8% and 2.8%, except one sample (TC-2) that has a high value of 3.5%. The average K% of loess samples from Asia is 1.890 ± 0.005% ($n = 2398$), and the regional average K content of loess and paleosol samples from Western Asia, Central Asia, Tibetan Plateau, Chinese Central Loess Plateau, NE China, Shandong Peninsula and Western Siberia is 1.84 ± 0.03 (%) ($n = 104$), 2.02 ± 0.01 (%) ($n = 528$), 1.83 ± 0.01 (%) ($n = 537$), 1.86 ± 0.01 (%) ($n = 868$), 2.18 ± 0.02 (%) ($n = 66$), 1.81 ± 0.02 (%) ($n = 238$) and 1.74 ± 0.03 (%) ($n = 58$), respectively (Fig. 2c). The concentration of Rb in loess samples from Central Asia and the Tibetan Plateau varies between 65 and 140 ppm, with an average of 97.34 ± 0.74 ppm ($n = 327$) (Fig. 2d). There is no substantial trend of U, Th, K and Rb concentration changes for loess samples from western Asia to central and eastern Asia, as well as for loess samples from different latitude from western Siberia to Tibetan Plateau.

The observed water content of loess samples from Western Asia to Central and Eastern Asia varies from 0 to 25%, except a few samples that have a slightly higher water content of 25–40%. The average water content of all loess samples from across mid-latitude Asia is 10.63 ± 4.00% ($n = 700$) (Fig. 3). The life-average water content used in dose rate calculation basically varies between 5 and 25%, with an average value of 11.66 ± 4.66% ($n = 2328$), which is fundamentally consistent with the average observed water content of 10.63 ± 4.33% ($n = 700$). Thus, indicating the suitability of life-average water content used in dose rate calculation. The calculated dose rates of different grain size quartz and -feldspar by using the radioactive element concentration of U, Th, K and Rb and water content is shown in Fig. 4. The calculated dose rate of most 63–90 μm size quartz samples varies between 2.2 and 4.3 Gy ka^{-1} with an average of 3.06 ± 0.01 Gy ka^{-1} ($n = 631$), the calculated dose rate of most 38–63 μm size quartz samples varies between 2.5 and 5.5 Gy ka^{-1} with an average of 3.49 ± 0.04 Gy ka^{-1} ($n = 248$), and the calculated dose rate of most 4–11 μm size quartz samples varies between 2.5 and 4.6 Gy ka^{-1} with an average of 3.69 ± 0.02 Gy ka^{-1} ($n = 386$). While the calculated dose rate for 63–90 μm size K-feldspar samples varies between 2.5 and 4.7 Gy ka^{-1} with an average value of 3.53 ± 0.01 Gy ka^{-1} ($n = 610$), the calculated dose rate for 38–63 μm size K-feldspar samples varies between 3.4 and 4.2 Gy ka^{-1} with an average value of 3.68 ± 0.06 Gy ka^{-1} ($n = 14$), and the calculated dose rate for 4–11 μm size K-feldspar samples varies between 3.1 and 5.7 Gy ka^{-1} with an average value of 4.18 ± 0.06 Gy ka^{-1} ($n = 99$); these values are slightly higher compared to quartz samples due to internal dose rate contribution from K and Rb in K-feldspar grains.

The 1785 quartz OSL ages on loess samples from 121 loess sections in Asia range from 0.1 to 115.0 ka, where most ages are less than 80 ka (Fig. 5). The error on most loess quartz OSL ages vary between 3 and 10%, and has an average error of 7.18 ± 0.08 (%) ($n = 1785$). A high error of 10–44% has been observed for young samples with ages less than 2 ka, which is likely due to the weak luminescence signal of young samples and the systematic errors related to quartz OSL dating.

A total of 921 pIRIR ages (including $pIR_{50}IR_{290}$ and $pIR_{200}IR_{290}$ ages) were compiled on loess samples from 12 sections and ranges from 2 to 300 ka. Here, only 2 samples have an age of less than 2 ka, while the ages of the 866 samples are larger than 10 ka (Fig. 6). All ages larger than 250 ka are considered as minimum ages due to the saturation and/or near saturation of the pIRIR signals, which can be seen in the pIRIR ages older than 250 ka, that have not shown an obvious increase with depth in QS16 and ZD17 from Central Asia and JingbianA–E sections from Chinese Central Loess Plateau. The error on most $pIR_{200}IR_{290}$ ages of K-feldspar samples generally varies between 1 and 10%, except a few high values of 10–45% for ages less than 10 ka (Fig. 6b). The average error on $pIR_{200}IR_{290}$ ages for all samples are 5.45 ± 0.13% ($n = 642$). The $pIR_{50}IR_{290}$ ages of loess samples from Western Asia, Central Asia, NE China, Shandong Peninsula and Western Siberia mostly range from 3 to 141 ka (Fig. 6a). The error on most K-feldspar $pIR_{50}IR_{290}$ ages varies between 2 and 21%, and has an average error of 6.66 ± 0.13% ($n = 279$). The 5 youngest samples in the pIRIR age dataset have a large error of 10–20%, compared to the other 266 samples, that have an error of less than 10%.

As illustrated in Fig. 6c, the 117 $pIR_{50}IR_{170}$ ages from sections LJW10 and NLT17 from the Tianshan Mountain region, sections HS18, Hebei and LD from NE Tibetan Plateau, and section XZP

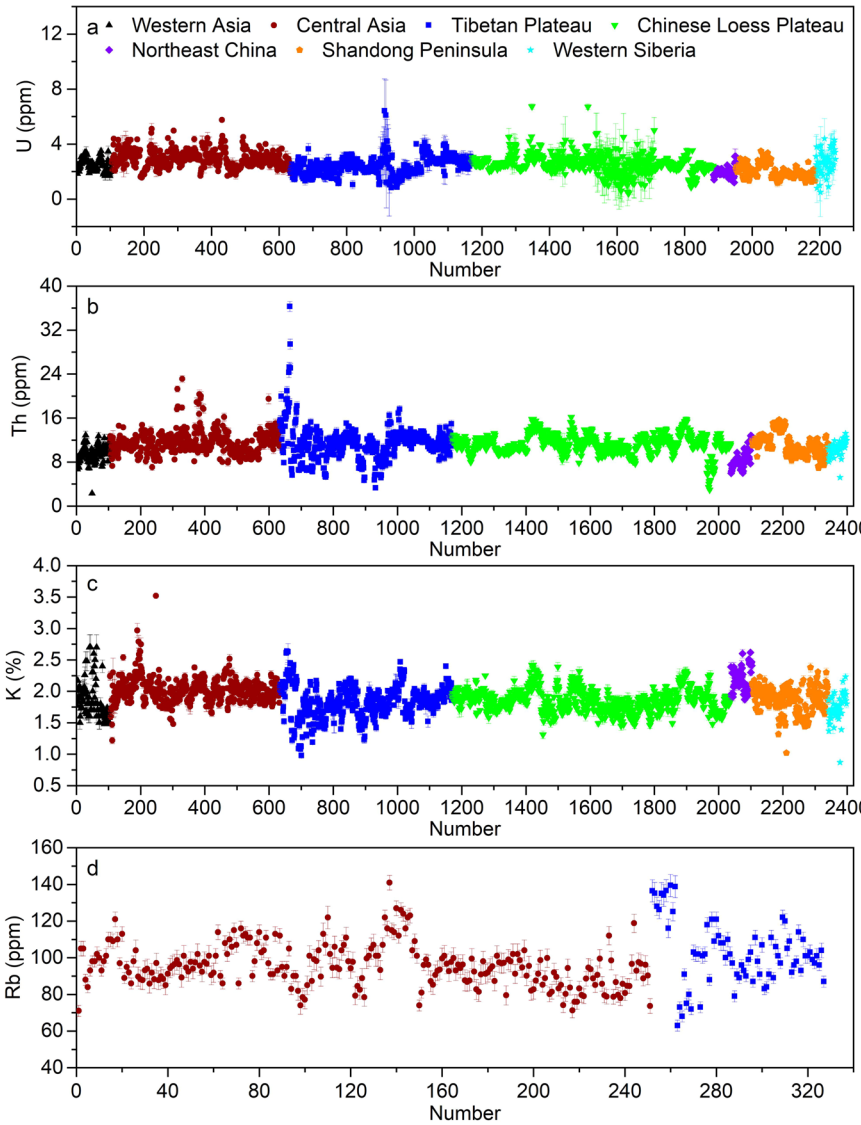

Fig. 2 **The summary of concentrations of radioactive elements data for loess samples from different regions of Asia. a–d** is U, Th, K, and Rb concentrations, respectively.

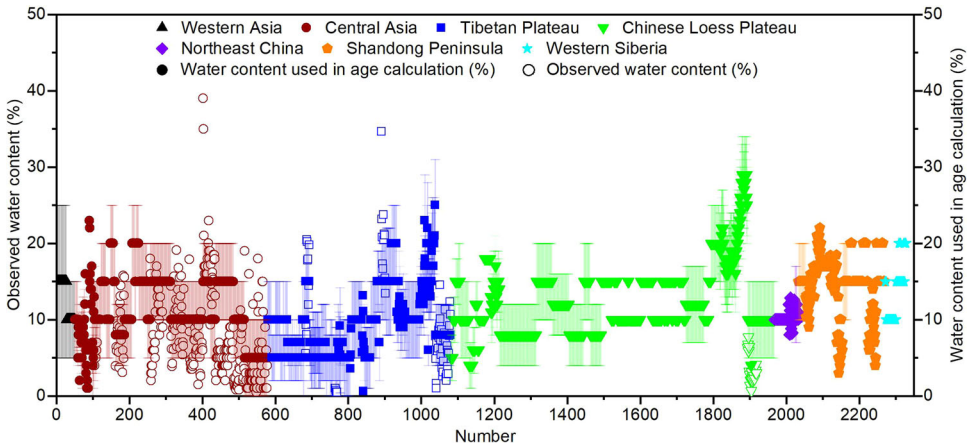

Fig. 3 The observed water content and water content used in age calculation for loess samples from different regions of Asia.

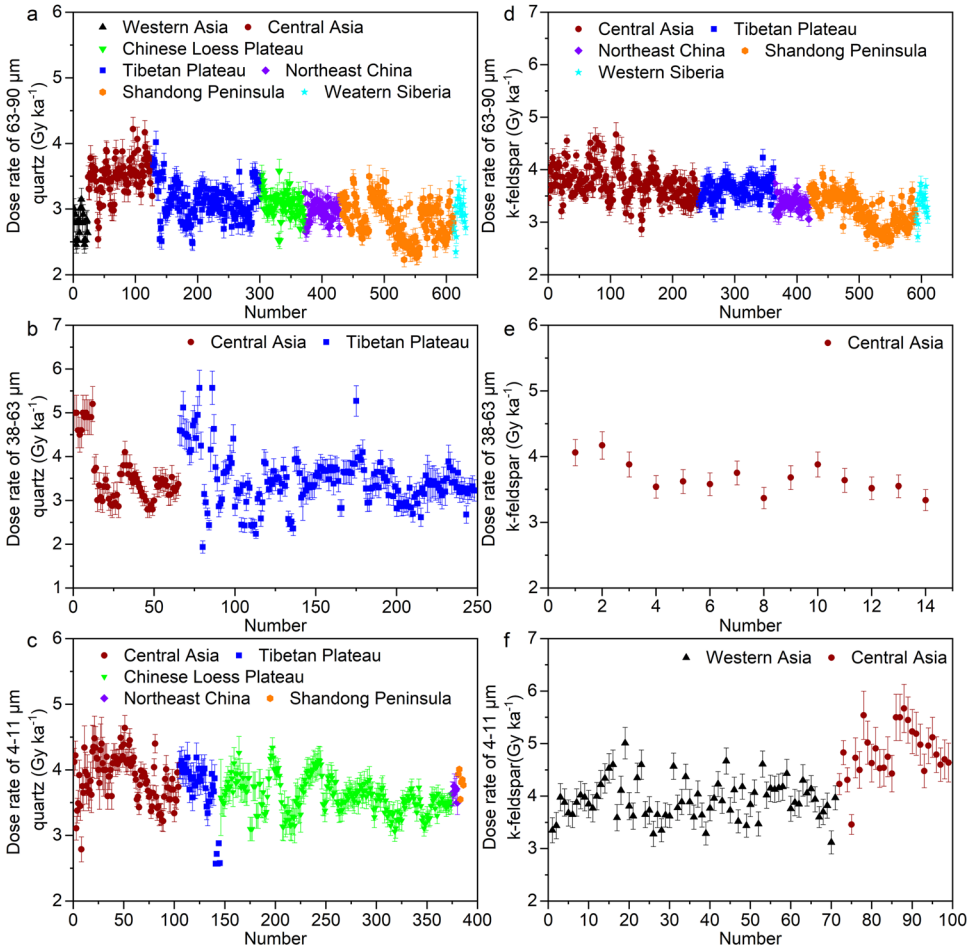

Fig. 4 The summary of dose rate data of samples from loess-paleosol sequences in different regions of Asia. a–c are the dose rate data of 63–90, 38–63 and 4–11 μm quartz samples, respectively. **d–f** are the dose rata data of 63–90, 38–63 and 4–11 μm K-feldspar samples, respectively.

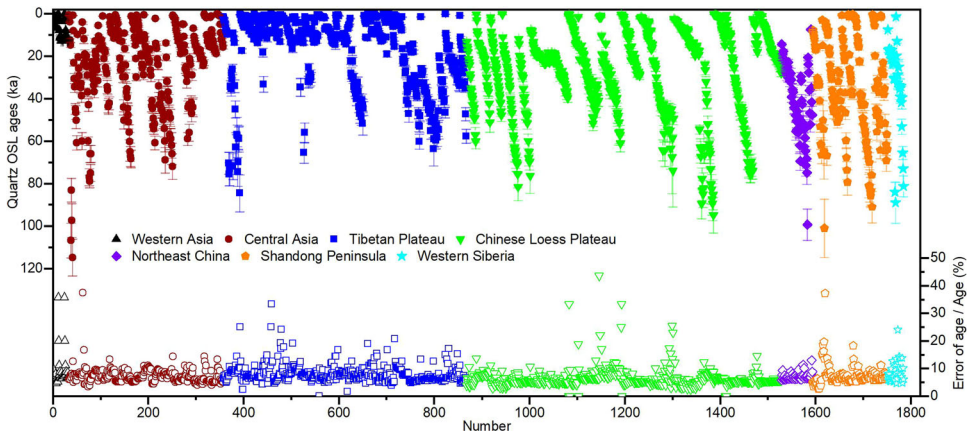

Fig. 5 The quartz OSL ages (solid symbol) and relative error of ages (hollow symbol) of samples from loess-paleosol sections in different regions of Asia.

from Shandong Peninsula ranges from 0.4 to 76.0 ka, where most of ages are less than 50 ka. The $pIR_{50}IR_{170}$ ages larger than 50 ka can be used as minimum ages due to the underestimation of $pIR_{50}IR_{170}$ signal for samples larger than 50 ka[33,39]. The error on most $pIR_{50}IR_{170}$ ages of K-feldspar samples generally vary between 4 and 8%, and has an average error of 6.29 ± 0.49% ($n = 117$). The error on 7 very young samples of ages less than 4 ka, varies between 8 and 50%, and shows an obvious increase compared to relatively older samples.

A total of 38 age-depth model were generated for loess-paleosol sequences from Asia, including 22 from Central Asia (sections ZSP, Zhaosu, SG18, Xiaoerbulake, Talede, XEBLK, KETB, XY17, NLK, ZD17A, ZD17B, ZD17C, ZD17D, KS15, NLT17, LJW10, QS16, BYH10, CJB21-1, CJB21-2, BG21-1 and XG21-1), 3 from Tibetan Plateau (sections XY18, RYS17 and HS18), 10 from Chinese

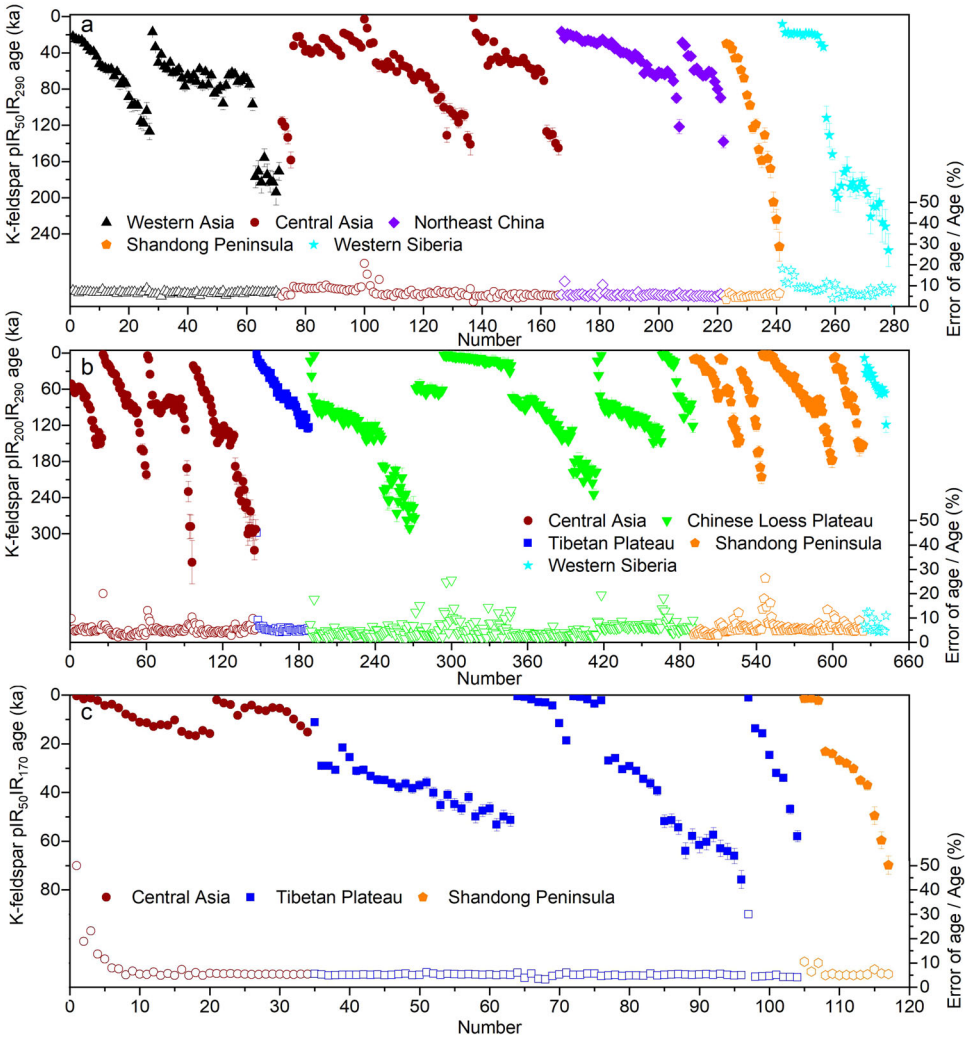

Fig. 6 The summary of K-feldspar pIRIR ages for samples from loess-paleosol sections in different regions of Asia. a is the K-feldspar $pIR_{50}IR_{290}$ ages (solid symbol) and relative error of ages (hollow symbol). **b** is the K-feldspar $pIR_{200}IR_{290}$ ages (solid symbol) and relative error of ages (hollow symbol). **c** is the K-feldspar $pIR_{50}IR_{170}$ ages (solid symbol) and relative error of ages (hollow symbol).

Central Loess Plateau (sections GL, Longgugou, JingbianA, JingbianB, JingbianC, JingbianD, JingbianE, WN2, WN and GB), and 2 from Shandong Peninsula (Sections FoCun2 and ShaoZhuang), and 1 from Western Siberia (section Solonovka). Age-depth models were generated at 1–2 cm intervals and span the past 250 ka. All age-depth models for loess sequences are generated considering the discontinuity in deposition due to hiatus in ages with depth, which becomes apparent with high-resolution luminescence dating of loess-paleosol sequences[2,9,10,16,17,25,27,30,41]. The error on age-depth modeling of loess-paleosol sequences varies between 1 and 7% for Pleistocene records, and yields an average error of 3.52 ± 0.23% ($n = 36$). By contrast, the error on age-depth modeling of loess-paleosol sequences varies 2–18% for Holocene records, with an average error of 8.84 ± 0.90% ($n = 25$).

The comparison of quartz OSL age and K-feldspar pIRIR ages, including $pIR_{50}IR_{290}$ and $pIR_{200}IR_{290}$ ages, for loess samples from different regions of Asia show that they are generally consistent with each other for samples less than ~50 ka, consequently re-affirming the reliability of quartz OSL and K-feldspar pIRIR ages for samples less than ~50 ka. However, for samples older than 50 ka, quartz OSL ages show an obvious underestimation compared to K-feldspar $pIR_{50}IR_{290}$ and $pIR_{200}IR_{290}$ ages; most likely caused by the instability and/or saturation of quartz OSL signal in the high dose region. The underestimation of quartz OSL ages for samples older than 50 ka is commonly observed for loess samples from Asia, which is likely caused by the offset of the natural signal generated dose response curve compared to the laboratory dose generated dose response curve in high dose regions (>200 Gy)[29,42]. The K-feldspar $pIR_{50}IR_{170}$ ages are generally consistent with quartz OSL ages, but obvious underestimation can be seen compared to K-feldspar $pIR_{200}IR_{290}$ ages for samples older than 40–50 ka, most likely caused by the instability of the $pIR_{50}IR_{170}$ signal for old samples. As such, quartz OSL and K-feldspar $pIR_{50}IR_{170}$ ages less than 40 ka can be used for loess-paleosol chronology determination, while the quartz OSL and K-feldspar $pIR_{50}IR_{170}$ ages older than 50 ka are used as minimum ages in chronology determination (Fig. 7).

The mean grain size of loess-paleosol sequences from mid-latitude Asia varies between 15 and 60 μm, with an average mean grain size of 31.41 ± 0.12 μm ($n = 13,651$), which shows that loess in Asia is dominated by silt. Notable exceptions to this are loess samples from XY18 and Sagaxi sections in the Tibetan Plateau and the SBH section in NE China that has a mean grain size of 60–150 and 60–100 μm respectively. In general, the sand component (>63 μm, %) shows consistent variation with mean grain size (Fig. 8). The sand fraction of loess in Asia generally varies between 0 and 40%, with an average of 15.92 ± 0.14 μm (%) ($n = 8458$), while

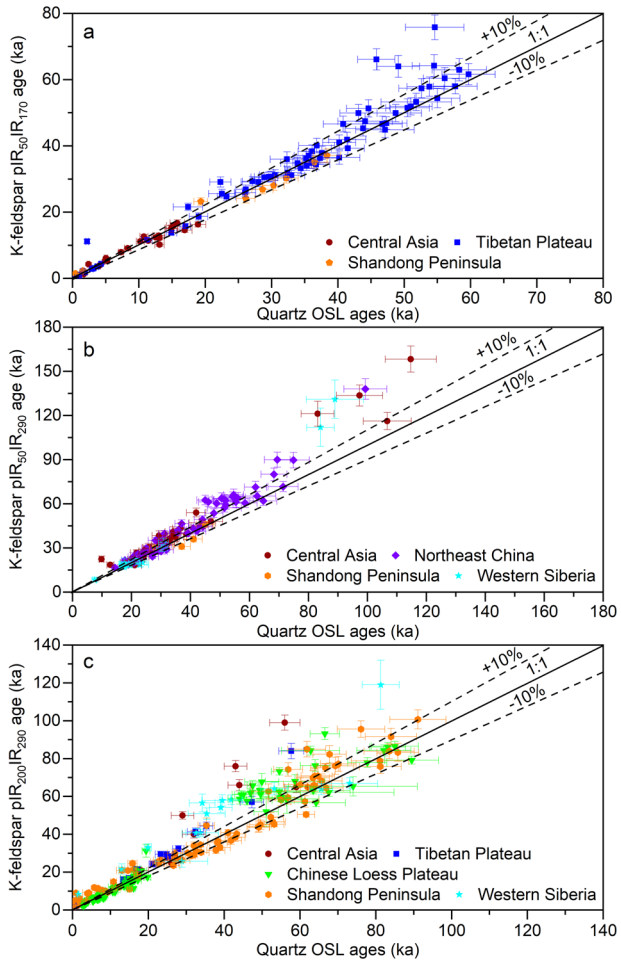

Fig. 7 The comparison of K-feldspar pIRIR ages and quartz OSL ages for loess samples from different regions of Asia. a is the comparison of $pIR_{50}IR_{170}$ ages and quartz OSL ages. **b** is the comparison of $pIR_{50}IR_{290}$ ages and quartz OSL ages. **c** is the comparison of $pIR_{200}IR_{290}$ ages and quartz OSL ages.

the samples of sandy loess at sections XY18 from the Tibetan Plateau, TJD from Shandong Peninsula and SBH from NE China have a high value of 40–80%. The silt component (2–63 μm, %) of loess in Asia generally varies between 60 and 90%, with an average of 74.96 ± 0.13 μm (%) ($n = 7897$) of silt in Asian loess samples. The clay component (<2 μm, %) of loess in Asia is generally less than 25%, with an average of 8.70 ± 0.05 μm (%) ($n = 7,899$) of clay in Asian loess samples, with the exception of the NLT17 section in Arid Central Asia that has a comparatively higher clay content of 25–40%[17]. There is no obvious trend for the variation of mean grain size, sand, silt and clay components of loess samples from western to central and eastern Asia, as well as from western Siberia to Central Asia and Tibetan Plateau (Fig. 8).

The magnetic susceptibility of loess deposits reflects the type, concentration, and grain size of magnetic minerals comprising the sediment[1]. In high precipitation regions (with precipitation of more than 400 mm y^{-1}), magnetic enhancement is mainly related to the formation of ferri and ferromagnetic minerals during post-depositional pedogenesis, therefore, the χ_{lf} variation was used as an indicator of pedogenesis controlled by the availability of effective moisture[43]. In drier areas of Central Asia (with precipitation less than 400 mm y^{-1}), χ_{lf} of loess deposits is interpreted as largely relating to the grain-size distribution of magnetic minerals, which has a close relationship to wind intensity and presence input of magnetic minerals, rather than the pedogenic processes[44]. However, the parameter χ_{fd} is sensitive to the content of super-paramagnetic (SP) grains <0.03 μm that are controlled by pedogenic intensity[45], making χ_{fd} a reliable proxy index for pedogenesis and effective moisture in both relatively dry and moist areas of Asia[16]. The χ_{lf} is generally less than 160 (10^{-8} m^3 kg^{-1}) for most loess samples from Western and Central Asia[2], but shows an obvious increase to 200–300 (10^{-8} m^3 kg^{-1}) for loess samples from the Chinese Central Loess Plateau and eastern China[14]. The average χ_{lf} values of loess samples from Western and Central Asia are 63.60 ± 0.28 (10^{-8} m^3 kg^{-1}) ($n = 8054$), which can be attributed to a mostly arid environment in these regions. The average χ_{lf} values of loess samples from Chinese Central Loess Plateau and Shandong Peninsula of eastern China are 76.38 ± 0.82 (10^{-8} m^3 kg^{-1}) ($n = 5601$), which is slightly higher compared to Western and Central Asia; which most likely occurs due to a relatively moist environment in these regions. The χ_{fd} values of samples from loess-paleosols of mid-latitude Asia varies between 0 and 12% with an average value of 1.47 ± 0.02 (%) ($n = 8262$), and has relatively higher values for paleosols and lower values for loess units, thus indicating generally weak pedogenesis and low effective moisture in mid-latitude Asia. The relatively high χ_{fd} values of 4–10% are mostly observed in loess samples from intermountain basins and high mountain regions of Western and Central Asia, and monsoonal NE China and Shandong Peninsula (Fig. 9).

Carbonates in loess sequences consist of primary carbonate (e.g., calcite and dolomite) and secondary (or pedogenic) carbonates (mainly calcite) that is formed after deposition. Increased precipitation induces leaching and reprecipitation processes of carbonate during pedogenesis[46], thus carbonate content can be used as an indicator of precipitation in the region[47]. Increased precipitation would cause strong leaching and thus high carbonate content in loess below the paleosol unit, while low precipitation would result in weak leaching and therefore low carbonate content in the loess unit. The $CaCO_3$ content of loess samples from mid-latitude Asia varies between 5 and 24%, except for loess samples from the NLT17 section from Central Asia and WN section from Chinese Central Loess Plateau that yield values of <5%. The average $CaCO_3$ content is 12.35 ± 0.09% ($n = 2204$) for all loess samples from Asia. There is no obvious trend in $CaCO_3$ content for loess samples from Central Asia to Tibetan Plateau and Chinese Central Loess Plateau (Fig. 9).

Redness (a*) of loess and paleosol sediments is controlled by the content of hematite and other observed iron hydroxides[48–50]. Thus, relative redness can be used to reflect the relative degree of chemical weathering of sediments[12]. Under warm and humid conditions, Fe^{2+} is oxidized to Fe^{3+} and eventually incorporated into stable hematite or goethite, resulting in reddish paleosols and a higher a* value[51]. High redness of loess-paleosol sequences from mid-latitude Asia is related to strong chemical weathering and pedogenesis under a warm and moist environment[52]. The yellowness (b*) is affected by the mass fraction of goethite, as well as iron minerals such as pyrite, marsh iron ore and limonite, that can reflect the relative change in precipitation in the region[49,50]. The lightness (L) is related to the content of TOC and $CaCO_3$, such that an increase of $CaCO_3$ and decrease of TOC would cause a high L value, and can therefore, be used as an indicator of vegetation and precipitation changes in the region[52,53]. The variation in Lightness (L) parameter of loess-paleosol sequences decreases slightly from Western and Central Asia to Shandong Peninsula of eastern China. In contrast the variation of a* and b* in loess-paleosol sequences shows an obvious increase from Central Asia and Qinghai-Tibetan Plateau to Shandong Peninsula, as a result of increasing precipitation from arid inland Asia to monsoonal East Asia (Fig. 10). The a* values of loess samples in Asia varies between 1 and 9%, with an average of 4.00 ± 0.02% ($n = 3321$), while the b* values of loess samples ranged from 1 to 30%, with an average of 16.65 ± 0.08 (%)

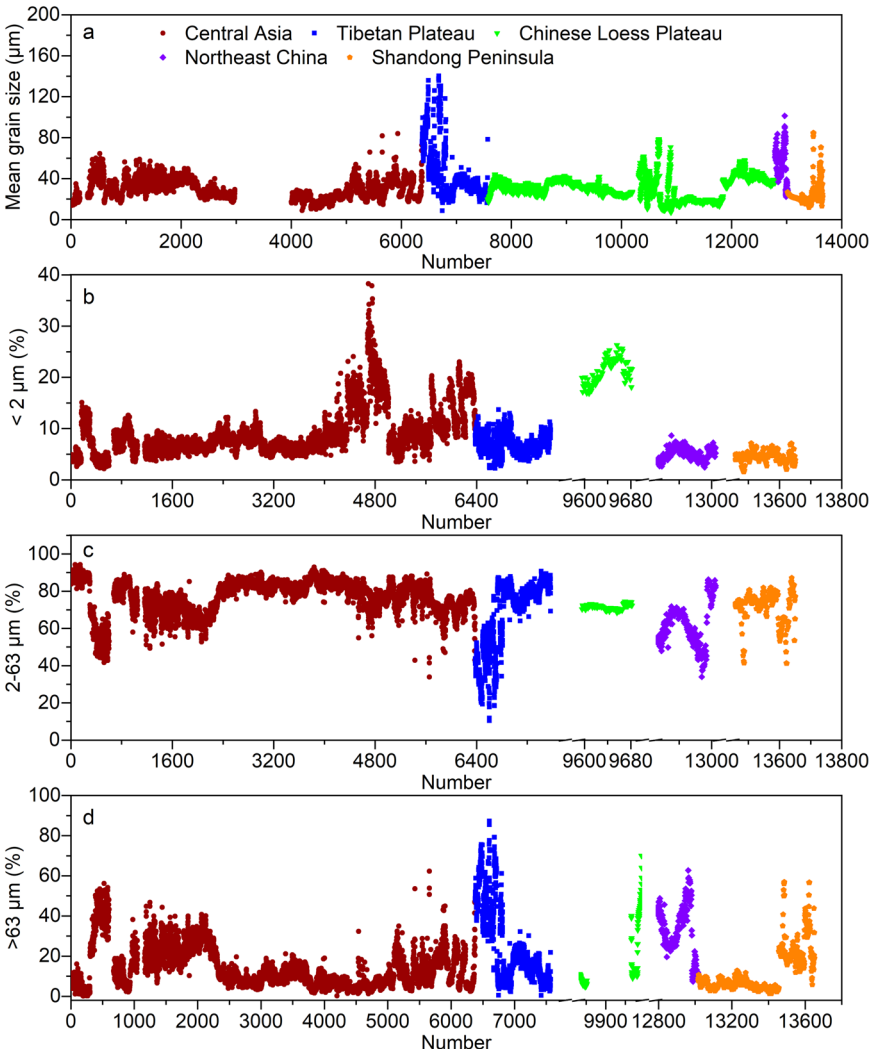

Fig. 8 The summary of grain size data of samples from loess-paleosol sections in different regions of Asia. a–d are the mean grain size, silt, clay, and sand component changes, respectively.

($n = 3237$). The lightness (L) of loess samples from Asia varies between 20 and 78%, with an average value of 60.61 ± 0.15 (%) ($n = 3326$). The L parameter does not show any obvious trend across different geographical regions of mid-latitude Asia, which is most likely caused by poor vegetation and low precipitation changes in the mostly arid and semi-arid loess depositional regions of mid-latitude Asia.

We compiled a comprehensive dataset of previously published environmental proxy indices of grain size, magnetic susceptibility, $CaCO_3$, Chroma reflection and luminescence ages as well as reconstructed age-depth models for loess-paleosol sequences from different regions of Asia. The dataset comprises 1785 quartz OSL ages and 1038 K-feldspar pIRIR ages from 128 loess-paleosol sequences spanning the past 300 ka and 12,365 grain size, 14,964 magnetic susceptibility, 2204 $CaCO_3$, and 3326 chroma data from 51 loess-paleosol sequences. This dataset provides the most detailed overview of luminescence ages and environmental proxy indices for loess-paleosol sequences across Asia. The loess-paleosol sequences compiled here, covers a large geographic extent, with different elevations, diverse geomorphic settings and climatic systems of mid-latitude westerlies and low-latitude EASM and EAWM, which makes the dataset qualified for large-scale studies across the Asia. The age data from the loess-paleosol sequences can be used to calculate the dust depositional rate of loess across different regions of Asia, thus providing fundamental input related to dust contribution as boundary conditions for paleoclimatic modeling over different timescales over the past 300 ka. The proxy indices dataset consisting of grain size, magnetic susceptibility, $CaCO_3$, and chroma reflection can be used to analyze the characteristics of loess and paleosols across different regions of Asia over different timescales. This systematic dataset can provide important information on loess formation and depositional processes as well as paleoclimatic reconstructions in different climatic and geomorphological settings, that can help us understand the how the interplay of the EASM and westerlies influence climatic changes over mid-latitude Asia over glacial-interglacial cycles. Considering its broad spatial and temporal coverage, this dataset can serve as an important data source for understanding the processes and mechanism of desertification of inland Asia, and for forecasting the impact of future climatic changes (e.g., warming) on desertification at regional and global scales.

METHODS

Laboratory measurements of luminescence dating of Asian loess

All luminescence ages compiled in this paper, were pretreated and measured under subdued red or/and yellow light conditions

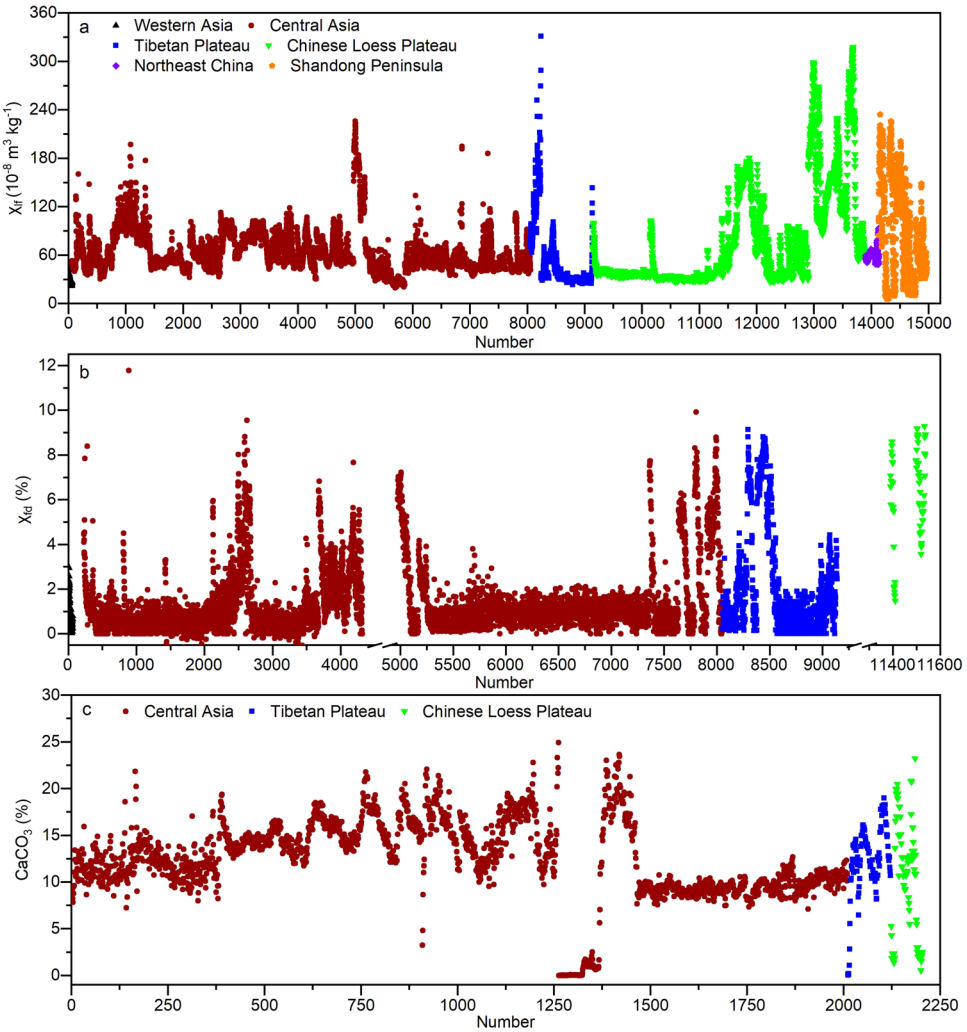

Fig. 9 The summary of magnetic susceptibility and $CaCO_3$ content of samples from loess-paleosol sections in different regions of Asia. **a**–**c** is the χ_{lf}, χ_{fd}, and $CaCO_3$ content changes, respectively.

in various Luminescence dating laboratories across the world. In general, luminescence samples were collected in opaque tubes. The bulk material from the light-exposed ends of the tubes was used to determine radioelement content for dose-rate analysis. The remaining sample was treated with 10% HCl and 10–20% H_2O_2 to remove carbonate and organic materials respectively, and then wet-sieved to retrieve the different grain size fractions of <38 or <63 µm, 38–63 µm, 63–90 and 90–125 µm. Following which standard heavy liquid separation was performed for the different grain size fractions using densities of 2.75, 2.62 and 2.58 g cm^{-3} to separate heavy minerals, quartz and K-feldspar fractions, respectively. The quartz fraction was further treated with 40% HF for at least 40 min to remove the outer layer impacted by alpha radiation along with any remaining feldspar grains. In some cases, K-feldspar grains were also treated by digestion in 10% HF for 10–40 min to remove the outer layer affected by alpha radiation. Both quartz and K-feldspar fractions were finally treated with 1 mol L^{-1} HCl for 10–15 min to remove fluorides created during the HF etching. The fine grain (4–11 µm) quartz samples were prepared by settling the <63 or <38 µm sieved fraction using stokes law. The resulting fine grain polymineral fraction was further etched with hexafluorosilicic acid for 7–14 days to obtain fine grain quartz.

Luminescence measurements were conducted on Risø-TL/OSL-DA-20 readers equipped with blue LEDs (470 nm, ~80 mW cm^{-2}) and IR LEDs (870 nm, ~135 mW cm^{-2}) or/and Daybreak 2200 OSL reader equipped with blue (470 ± 5 nm) LED units and IR LEDs (880 ± 60 nm). Laboratory irradiation was carried out using $^{90}Sr/^{90}Y$ sources mounted on the reader, with a calibrated dose rate of ~0.08–0.13 Gy ka^{-1}. The quartz OSL signal was detected using a 7.5 mm Schott U-340 glass filter, while the K-feldspar IRSL signals were detected through a combination of BG-39 and Corning-759 filters.

For quartz OSL dating sample, the purity of each sample was checked by using IR-depletion tests and/or IR/OSL signal ratio[54]. The quartz OSL equivalent dose (D_e) values were measured by using single-aliquot regeneration (SAR) protocols[55], or a combination of SAR and SGC (Standardized Growth Curve) measurements[56]. The fine-grained quartz sensitivity-corrected multiple-aliquot regenerative-dose (SMAR) OSL dating protocol was used for D_e determination of samples from the Weinan (WN) section, China[57]. The double-single-aliquot regeneration protocol[58] (DSAR), which includes an IR irradiation prior to OSL measurement in each cycle of the SAR protocol, was used to evaluate D_e values from fine grains from Remizovka (REM), Panfilov (PAN) and Ashubulak (ASH) from Central Asia[32]. Dose recovery tests were conducted on representative samples of each loess-paleosol section to select suitable preheat temperature for D_e measurement and check the reliability of SAR protocol to loess samples from different regions.

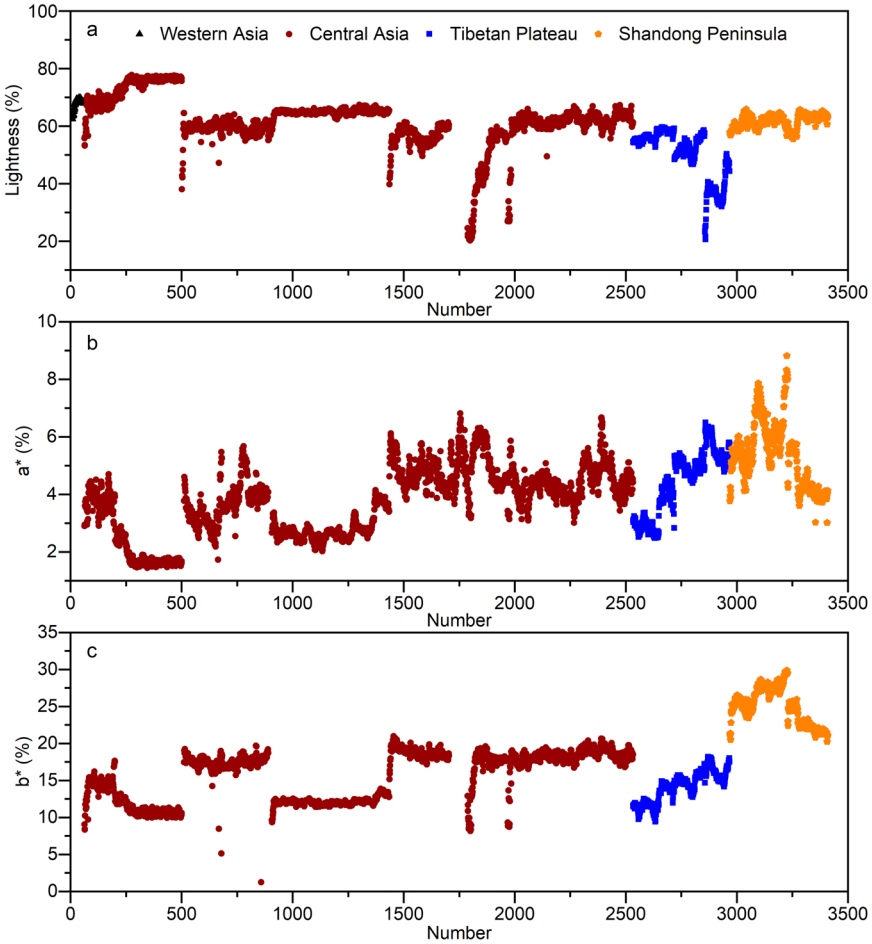

Fig. 10 The summary of color reflection changes of samples from loess-paleosol sections in different regions of Asia. a–c is the lightness, redness, and yellowness changes, respectively.

Six to thirty aliquots of each sample were analyzed for determination of D_e, and consequently the age of the sample.

The total dose rate of each quartz sample was calculated from measurements of radioactive element concentrations in the sample, with a small contribution from cosmic rays. The U, Th, K and Rb concentrations of each sample was determined using either Neutron Activation Analysis (NAA), Inductively-coupled plasma mass spectrometry (ICP-MS), inductively-coupled plasma optical emission spectroscopy (ICP-OES) or high-resolution gamma spectrometry. The dose rate contribution from Rb concentrations is very small (e.g., <1%) (and has been ignored in dose rate calculations for samples from most sections, except sections SG18, XY17, ZD17, KS15, NLT17, LJW10, BYH10 and QS16 from Tianshan Mountain regions and sections CJB21-1, CJB21-2, BG21-1 and XG21-1 from Hexi corridor of Central Asia, and sections XY18, RYS17, Sagaxi, and HS18 from NE Tibetan Plateau, and Zouyu section from Shandong Peninsula. Conversion factors were used to convert measured radioactive element concentrations to beta and gamma dose rates[59]. The cosmic dose rate of each sample is calculated using the sample burial depth and the altitude and elevation of the loess section according to Prescott and Hutton (1994)[60]. The life-average water content of loess samples from each section were estimated based on the observed water content, and the uncertainty of water content changes after burial, taking in account the slight loss of sample moisture that occurs naturally during sampling and transport. The OSL age of each quartz sample was calculated by using the ratio of measured quartz D_e value to the annual dose rate[23].

The K-feldspar pIRIR dating method, utilizing the $pIR_{50}IR_{290}$ signal[36], $pIR_{200}IR_{290}$ signal[61], and $pIR_{50}IR_{170}$ signal[62] was used to coarse-grained (e.g., 63–90 μm) and fine-grained (e.g., 4–11 μm) K-feldspar samples from loess sections. The $pIR_{50}IR_{290}$ signal and $pIR_{200}IR_{290}$ signal dating can be used to date samples with ages ranges from few ka to 130–150 ka, and few ka to 250–300 ka, respectively, while the $pIR_{50}IR_{170}$ signal dating can be used to date young samples from few hundred years to tens of thousands of years[17,62]. In the $pIR_{50}IR_{290}$ and $pIR_{200}IR_{290}$ dating protocols, a preheat of 320 °C for 60 s was followed by an IRSL stimulation at 50 °C or 200 °C, which was followed by a high temperature IR stimulation at 290 °C. In the $pIR_{50}IR_{170}$ dating protocol, a preheat of 200 °C for 60 s was followed by IRSL stimulation at 50 °C. This was followed by a pIRIR measurement at a high stimulation temperature of 170 °C. In some cases, prior to all IRSL measurements, the aliquots were held at the measurement temperature for a few seconds without IR stimulation in order to reduce the intensity of the residual isothermal luminescence after preheating. In general, test doses between 30 and 50% of the D_e values of the sample were used in all pIRIR measurement protocols[7,63]. The suitability of pIRIR dating protocols using $pIR_{50}IR_{290}$, $pIR_{200}IR_{290}$ and $pIR_{50}IR_{170}$ signals for samples from each loess-paleosol sequence was checked using dose recovery tests on samples bleached in sunlight and/or modern analog samples[64]. Residual dose corrections on these K-feldspar ages were performed by conducting bleaching tests, wherein the residual pIRIR signals measured from samples bleached under sunlight or by a solar simulator are subtracted from the D_e value of each sample[36].

Total dose rate calculations for K-feldspar sample consisted of external dose rate of radioactive elements (U, Th, K and Rb) in the sample, internal dose rate of K-feldspar grains, and dose rate contribution from cosmic rays. Published conversion factors were used to convert measured radioactive element concentrations to beta and gamma dose rates[59]. Internal dose rates for K-feldspar samples were calculated using a K content of 12.5 ± 0.5%[65,66] and a Rb content of 400 ± 100 ppm[67]. The cosmic dose rate of each sample is calculated according to Prescott and Hutton[60] taking into account sample burial depth, and the altitude and elevation of the loess section. The life-average water content of loess samples from each section was estimated based on the observed water content, and the uncertainty of water content changes after burial, which is similar that performed for quartz samples. The pIRIR age of each sample was calculated as a ratio of the measured D_e value to the annual dose rate.

Age-depth modeling of loess-paleosol sequences in Asia

Both quartz and K-feldspar pIRIR dating generated individual ages at distinct depth intervals in the individual loess sequences. Construction of a continuous paleoclimatic record requires the development of an age-depth model that can be used to interpolate between these discrete ages. The age-depth model of loess sections was established using Bacon age-depth modeling[68], which uses Bayesian statistics to reconstruct accumulation histories for deposits, and can be used to reduce the size of age-depth model error estimates by considering the stratigraphic positions of the ages. The age-depth modeling of 22 loess-paleosol sections from central Asia, 10 sections from Chinese Central Loess plateau, 1 section from western Siberia and 3 sections from Tibetan Plateau, and 2 sections from Shandong Peninsula of eastern China, spanning the past 250–300 ka, was reconstructed based on close-spaced quartz OSL ages and/ or K-feldspar pIRIR ages from each section.

Grain size measurement

A total of 12,365 grain size samples collected from 46 loess-paleosol sections (sections Remizovka (REM), Panfilov (PAN), Ashubulak (ASH), ZSP, SGX, Zhaosu, SG18, Xiaoerbulake, Talede, XEBLK, KETB, XY17, NLK, ZD17, KS15, NLT17, LJW10, QS16, BYH10, CJB21-1, CJB21-2, BG21-1 and XG21-1 from Central Asia, sections Sagaxi, SNP, LXP, YJP1, XY18, RYS17 and HS18 from the Tibetan Plateau, sections GL, JY12, BGY Holocene site, Xifeng, XF06, Longgugou, JingbianA–E, WN2, WN and GB sections from the Chinese Central Loess Plateau, sections SBH and NYZG from Northeastern China, and sections FoCun2, ShaoZhuang, LGZ and TJD from Shandong Peninsula) from Central and East Asia were analyzed.

For grain size analyses, in most cases sediment samples were heated with 10 ml of 30% H_2O_2 and 10 ml of 10% HCl to remove organic matter and carbonate material. The sample was then suspended in deionized water for 24 h to remove acidic ions. Following this, the samples were deflocculated using 10 ml of 0.1 mol L^{-1} $(NaPO_3)_6$ in an ultrasonicator for 10 min[69]. Prepared samples were then measured using a Malvern Master Sizer 2000 with a range of 2–2000 µm, or using a CILAS 1190 LD laser particle analyzer with a range of 0.04–2500 µm.

Magnetic susceptibility measurement

A total of 14,964 magnetic susceptibility samples collected from 46 loess-paleosol sections (Section YE from Western Asia, sections Remizovka (REM), Panfilov (PAN), Ashubulak (ASH), ZSP, Zhaosu, SG18, Xiaoerbulake, Talede, XEBLK, KETB, XY17, NLK, ZD17, KS15, NLT17, LJW10, QS16, BYH10, CJB21-1, CJB21-2, BG21-1 and XG21-1 from Central Asia; sections Sagaxi, YJP1, XY18, RYS17 and HS18 from Tibetan Plateau; sections GL, JY12, BGY Main site, BGY Holocene site, Xifeng, XF06, Longgugou, Xunyi, JingbianA-E, WN2, WN and GB from Chinese Central Loess Plateau; sections SBH and NYZG from Northeastern China, and sections Yizheng, Maba, LGZ and TJD from Shandong Peninsula) from Asia were analyzed.

Samples were air dried and packed into 10 cc plastic pots. Low frequency (470 Hz) magnetic susceptibility (χ_{lf}) and high frequency (4700 Hz) magnetic susceptibility (χ_{hf}) measurements were carried out using a Bartington Instrument MS2B Meter or using a AGICO Kappabridge MFK2. The percentage of mass-specific frequency-dependent susceptibility (χ_{fd}) was calculated by using the function (1)[70].

$$\chi_{fd} = \frac{100 * (\chi_{lf} - \chi_{hf})}{\chi_{lf}} \quad (1)$$

$CaCO_3$ content measurement

A total of 2204 $CaCO_3$ content samples from 5 sections (sections SG18, XY17, ZD17, NLT17 and QS16) from Central Asia, 1 section from Tibetan Plateau (section RYS17) and 1 section from Chinese Central Loess Plateau (section WN) were analyzed. The total carbonate content of each air-dried sample was measured by the gasometric method after samples were air-dried. A solution of 10% HCl was added to weighed samples and the induced volume of CO_2 was measured by a U-tube manometer. The carbonate content ($CaCO_3$) was then calculated according to the CO_2 volume, temperature and atmospheric pressure when the sample was measured[71].

Chroma reflectance measurement

A total of 3326 samples were compiled for color reflectance from 17 loess-paleosol sections from Asia (section YE from Western Asia, sections ZSP, SGX, Zhaosu, SG18, Xiaoerbulake, Talede, XY17, ZD17, NLT17, QS16 from Central Asia, sections Sagaxi, YJP1, XY18 and RYS17 from Tibetan Plateau, and sections FoCun2 and ShaoZhuang from Shandong Peninsula of eastern China). In the laboratory, the samples were air-dried and ~0.5 g of each sample was extracted. The dry samples were grounded using a mortar and pestle. Sediment color was measured on each air-dried sample after samples were disaggregated. Measurements were conducted on a Konica- MinoltaCM700d color meter. Color reflectance, defined by CIE L*a*b*, where the measured color indices L* indicates lightness, that defines black at 0 and white at 100, while a* and b* refer to redness and yellowness in Red–yellow chromaticity[49,50].

DATA AVAILABILITY

The compiled dataset from previously published studies consisting of U, Th, K and Rb concentration, water content, dose rate, quartz and K-feldspar ages, age-depth models of loess-paleosol sequences, as well as the environmental proxy indices of mean grain size, clay, silt and sand components, magnetic susceptibility (χ_{lf}, χ_{fd}), $CaCO_3$, and Chroma reflection of loess-paleosol sequences from Asia are accessible at the National Tibetan Plateau/Third Pole Environment Data Center (https://doi.org/10.11888/Paleoenv.tpdc.300496)[41].

Received: 11 October 2023; Accepted: 19 December 2023;
Published online: 03 January 2024

REFERENCES

1. Heller, F. & Liu, T. S. Magnetostratigraphical dating of loess deposits in China. *Nature* **300**, 431–433 (1982).
2. Song, Y. G. et al. Spatio-temporal distribution of quaternary loess across central Asia. *Palaeogeogr. Palaeoclimatol. Palaeoecol.* **567**, 110279 (2021).
3. Li, Y. R., Shi, W. H., Aydin, A., Beroya-Eitner, M. A. & Gao, G. H. Loess genesis and worldwide distribution. *Earth Sci. Rev.* **201**, 102947 (2020).

4. Schaetzl, R. et al. Approaches and challenges to the study of loess-Introduction to the LoessFest Special Issue. *Quat. Res.* **89**, 563–618 (2018).
5. Lauer, T. et al. Luminescence-chronology of the loess palaeosol sequence Toshan, Northern Iran – a highly resolved climate archive for the last glacial-interglacial cycle. *Quat. Int.* **429**, 3–12 (2017).
6. Liu, T. S. *Loess and the Environment* (Science Press, Beijing, 1985) (In Chinese).
7. Yi, S. W. et al. A detailed post-IR IRSL dating study of the Niuyangzigou loess site in northeastern China. *Boreas.* **45**, 644–657 (2016).
8. Liu, X. J. et al. Distribution and fate of Tibetan Plateau loess. *Catena* **225**, 107022 (2023).
9. Zhao, Q. Y. et al. Luminescence chronology of loess-palaeosol deposits in the Central Shandong Mountains region: provenances and paleoclimate implications. *Quat. Geochronol.* **70**, 101296 (2022).
10. Volvakh, N. E. et al. First high-resolution luminescence dating of loess in Western Siberia. *Quat. Geochronol.* **73**, 101377 (2022).
11. An, Z. S. The history and variability of the East Asian paleomonsoon climate. *Quat. Sci. Rev.* **19**, 171–187 (2000).
12. Ding, Z. L. et al. The loess record in southern Tajikistan and correlation with Chinese loess. *Earth Planet. Sci. Lett.* **200**, 387–400 (2002).
13. Guo, Z. T. et al. Onset of Asian desertification by 22 Myr ago inferred from loess depositsin China. *Nature.* **416**, 159–163 (2002).
14. Maher, B. A. Palaeoclimatic records of the loess/palaeosol sequences of the Chinese Loess Plateau. *Quat. Sci. Rev.* **154**, 23–84 (2016).
15. Chen, F. H. et al. Westerlies Asia and monsoonal Asia: spatiotemporal differences in climate change and possible mechanisms on decadal to suborbital timescales. *Earth Sci. Rev.* **192**, 337–354 (2019).
16. Li, G. Q. et al. Differential ice volume and orbital modulation of Quaternary moisture patterns between Central and East Asia. *Earth Planet. Sci. Lett.* **530**, 115901 (2020).
17. Li, G. Q. et al. Paleoclimatic changes and modulation of East Asian summer monsoon by high-latitude forcing over the last 130,000 years as revealed by independently dated loess-paleosol sequences on the NE Tibetan Plateau. *Quat. Sci. Rev.* **237**, 106283 (2020).
18. Hatte, C., Pessenda, L. C., Lang, A. & Paterne, M. Development of accurate and reliable ^{14}C chronologies for loess deposits: application to the loess sequence of nussloch (Rhine valley, Germany). *Radiocarbon* **43**, 611–618 (2001).
19. Dodson, J. R. & Zhou, W. J. Radiocarbon dates from a Holocene deposit in southwestern Australia. *Radiocarbon* **42**, 229–234 (2000).
20. Pessenda, L. C. R., Gouveia, S. E. M. & Aravena, R. Radiocarbon dating of total soil organic matter and humin fraction and its comparison with ^{14}C age of fossil charcoal. *Radiocarbon* **43**, 596–601 (2001).
21. Geyh, M. A., Roeschmann, G., Wijmstra, T. A. & Middeldorp, A. A. The unreliability of ^{14}C dates obtained from buried sandy Podzols. *Radiocarbon* **25**, 409–416 (1983).
22. McGeehin, J. et al. Stepped-combustion ^{14}C dating of sediment: a comparison with established techniques. *Radiocarbon.* **43**, 255–261 (2001).
23. Aitken, M. J. *An Introduction to Optical Dating* (Oxford University Press, Oxford, UK, 1998).
24. Murray, A. et al. Optically stimulated luminescence dating using quartz. *Nat. Rev. Methods Primers* **1**, 72 (2021).
25. Stevens, T. et al. Ice-volume-forced erosion of the Chinese Loess Plateau global quaternary stratotype site. Nature. *Communications.* **9**, 983 (2018).
26. Sun, Y. B. et al. Influence of Atlantic meridional overturning circulation on the East Asian winter monsoon. *Nat. Geosci.* **5**, 46–49 (2012).
27. Kang, S. G. et al. Early Holocene weakening and mid-to late Holocene strengthening of the East Asian winter monsoon. *Geology* **48**, 1043–1047 (2020).
28. Yi, S. W. et al. High resolution OSL and post-IR IRSL dating of the last interglacial-glacial cycle at the Sanbahuo loess site (northeastern China). *Quat. Geochronol.* **30**, 200–206 (2015).
29. Buylaert, J. P. et al. Luminescence dating of old (>70 ka) Chinese loess: a comparison of single aliquot OSL and IRSL techniques. *Quat. Geochronol.* **2**, 9–14 (2007).
30. Li, G. Q. et al. Paleoenvironmental changes recorded in a luminescence dated loess/paleosol sequence from the Tianshan Mountains, arid central Asia, since the Penultimate Glaciation. *Earth Planet. Sci. Lett.* **448**, 1–12 (2016).
31. Qin, J. T. & Zhou, L. P. Luminescence dating of the Zeketai loess section in the Ili Basin, northwestern China: methodological considerations. *J. Asian Earth Sci.* **155**, 146–153 (2018).
32. Dave, A. K., Lisa, L., Scardia, G., Nigmatova, S. & Fitzsimmons, K. E. The patchwork loess of Central Asia: implications for interpreting aeolian dynamics and past climate circulation in piedmont regions. *J. Quat. Sci.* **38**, 526–543 (2023).
33. Wang, Y. X. et al. Quartz OSL and K-feldspar post-IR IRSL dating of loess in the Huangshui river valley, northeastern Tibetan plateau. Aeolian. *Research.* **33**, 23–32 (2018).
34. Thomsen, K. J., Murray, A. S., Jain, M. & Bøtter-Jensen, L. Laboratory fading rates of various luminescence signals from feldspar-rich sediment extracts. *Radiat. Meas.* **43**, 1474–1486 (2008).
35. Thiel, C. et al. Luminescence dating of the stratzing loess profile (Austria)-testing the potential of an elevated temperature post-IR IRSL protocol. *Quat. Int.* **234**, 23–31 (2011).
36. Buylaert, J. P. et al. A robust feldspar luminescence dating method for Middle and Late Pleistocene sediments. *Boreas.* **41**, 435–451 (2012).
37. Buylaert, J. P. et al. A detailed post-IR IRSL chronology for the last interglacial soil at the Jingbian loess site (northern China). *Quat. Geochronol.* **30**, 194–199 (2015).
38. Fitzsimmons, K. E. et al. A chronological framework connecting the early Upper Palaeolithic across the Central Asian piedmont. *J. Hum. Evol.* **113**, 107–126 (2017).
39. E, C. et al. Hebei loess section in the Anyemaqen Mountains, northeast Tibetan Plateau: a high-resolution luminescence chronology. *Boreas* **47**, 973–1244 (2018).
40. Marković, S. B. et al. Danube loess stratigraphy – towards a pan-European loess stratigraphic model. *Earth Sci. Rev.* **148**, 228–258 (2015).
41. Li, G. Q. et al. A comprehensive dataset of luminescence ages and proxy indexes of loess-paleosol deposits across Asia. National Tibetan Plateau Data Center. https://doi.org/10.11888/Paleoenv.tpdc.300496 (2023).
42. Chapot, M. S., Roberts, H. M., Duller, G. A. T. & Lai, Z. P. A comparison of natural- and laboratory-generated dose response curves for quartz optically stimulated luminescence signals from Chinese Loess. *Radiat. Meas.* **47**, 1045–1052 (2012).
43. Jia, J., Liu, X. B., Xia, D. S., Wei, H. T. & Wang, B. Magnetic property of loess strata recorded by Kansu profile in Tianshan Mountains. *J. Arid Land* **3**, 191–198 (2011).
44. Lu, H. H. et al. Late Quaternary loess deposition in the southern Chaiwopu Basin of the northern Chinese Tian Shan foreland and its palaeoclimatic implications. *Boreas* **45**, 304–321 (2016).
45. Zhou, L. P., Oldfield, F., Wintle, A. G., Robinson, S. G. & Wang, J. T. Partly pedogenic origin of magnetic variations in Chinese loess. *Nature* **346**, 737–739 (1990).
46. Zhao, J. B. $CaCO_3$ and sedimentary environment of loess strata. *Acta Sedimentol. Sin.* **11**, 136–146 (1993).
47. Song, Y. G. et al. Loess magnetic properties in the Ili Basin and their correlation with the Chinese Loess Plateau. *Sci. China Earth Sci.* **53**, 419–431 (2010).
48. Giosan, L., Flood, R. D., Grützner, J. & Mudie, P. Paleoceanographic significance of sediment color on western North Atlantic Drifts: II. Late Pliocene–Pleistocene sedimentation. *Mar. Geol.* **189**, 43–61 (2002).
49. Lukić, T. et al. A joined rock magnetic and colorimetric perspective on the Late Pleistocene climate of Orlovat loess site (Northern Serbia). *Quat. Int.* **334-335**, 179–188 (2014).
50. Lukić, T. et al. Initial results of the colorimetric indices of the oldest exposed pedocomplex (Titel loess plateau, Serbia). *Geol. Croat.* **76**, 73–85 (2023).
51. Diao, G. Y. & Wen, Q. Z. The migration series of major elements during loess pedogenesis. *Geol. Geochem.* **27**, 21–26 (1999).
52. Li, Y., Song, Y. G. & Wang, Q. S. Chroma characteristics in the Zhaosu loess section and its paleoclimatic significance. *J. Earth Environ.* **5**, 67–75 (2014).
53. Shi, P. H., Yang, T. B., Tian, Q. C. & Wang, J. Y. Chroma chracteristics in the loess-paleosol at Jingyuan section and its signification to paleocliamete. *J. Lanzhou Univ. Nat. Sci.* **48**, 15–23 (2012).
54. Duller, G. A. T. Distinguishing quartz and feldspar in single grain luminescence measurements. *Radiat. Meas.* **37**, 161–165 (2003).
55. Murray, A. S. & Wintle, A. G. The single aliquot regenerative dose protocol: potential for improvements in reliability. *Radiat. Meas.* **37**, 377–381 (2003).
56. Roberts, H. M. & Duller, G. A. T. Standardised growth curves for optical dating of sediment using multiple-grain aliquots. *Radiat. Meas.* **38**, 241–252 (2004).
57. Kang, S. G., Wang, X. L., Lu, Y. C. & Quartz, O. S. L. chronology and dust accumulation rate changes since the Last Glacial at Weinan on the southeastern Chinese Loess Plateau. *Boreas* **42**, 815–829 (2013).
58. Banerjee, D., Murray, A. S., Bøtter-Jensen, L. & Lang, A. Equivalent dose estimation from a single aliquot of polymineral fine-grains. *Radiat. Meas.* **33**, 73–93 (2001).
59. Güerin, G., Mercier, N. & Adamiec, G. Dose-rate conversion factors: update. *Ancient TL* **29**, 5–8 (2011).
60. Prescott, J. R. & Hutton, J. T. Cosmic ray contributions to dose rates for luminescence and ESR dating: large depths and long-term time variations. *Radiat. Meas.* **23**, 497–500 (1994).
61. Li, B. & Li, S. H. A reply to the comments by Thomsen et al. on——Luminescence dating of K-feldspar from sediments: a protocol without anomalous fading correction. *Quat. Geochronol.* **8**, 49–51 (2012).
62. Li, G. Q. et al. Quartz OSL and K-feldspar pIRIR dating of a loess/paleosol sequence from arid central Asia, Tianshan Mountains, NW China. *Quat. Geochronol.* **28**, 40–53 (2015).
63. Colarossi, D., Chapot, M. S., Duller, G. A. T. & Roberts, H. M. Testing single aliquot regenerative dose (SAR) protocols for violet stimulated luminescence. *Radiat. Meas.* **120**, 104–109 (2018).

64. Wallinga, J., Murray, A. & Duller, G. Underestimation of equivalent dose in single-aliquot optical dating of feldspars caused by preheating. *Radiat. Meas.* **32**, 691–695 (2000).
65. Mejdahl, V. Thermoluminescence dating: beta-dose attenuation in quartz grains. *Archaeometry* **21**, 61–72 (1979).
66. Huntley, D. J. & Baril, M. R. The K content of the K-feldspars being measured in optical dating or in Thermoluminescence dating. *Ancient TL.* **15**, 11–13 (1997).
67. Huntley, D. J. & Hancock, G. V. The Rb contents of the K-feldspar grains being measured in optical dating. *Ancient TL.* **19**, 43–46 (2001).
68. Blaauw, M. Methods and code for 'classical' age-modelling of radiocarbon sequences. *Quat. Geochronol.* **5**, 512–518 (2010).
69. Peng, Y. J., Xiao, J. L., Nakamura, T., Liu, B. L. & Inouchi, Y. Holocene East Asian monsoonal precipitation pattern revealed by grain-size distribution of core sediments of Daihai Lake in Inner Mongolia of north-central China. *Earth Planet. Sci. Lett.* **233**, 467–479 (2005).
70. Thompson, R. & Oldfield, F. *Environmental Magnetism.* 227 (Allen & Unwin, London, 1986).
71. Bascomb, C. L. A calcimeter for routine use on soil samples. *Chem. Ind.* **45**, 1826–1827 (1961).

ACKNOWLEDGEMENTS

This research is supported by the Fundamental Research Funds for the Central Universities (lzujbky-2021-ey22), the Gansu Province Outstanding Youth Fund (23JRRA1016), the National Natural Science Foundation of China (Grant No. 42071101), and Youth Innovation Promotion Association Chinese Academy of Sciences (Y2022102).

AUTHOR CONTRIBUTIONS

G.L. conceptualized this study. G.L. and Z.Y. established the dataset and written the first drift of the manuscript. G.L., Y.S., K.E.F., S.Y., S.K., C.E., T.S., Z. Lai, A.K.D., H.Y., Q.Z., J.-P.B., Y.W., X.L., Z. Ling, Q.C., H.W., L.W. and F.C. contributed and collated the data, and performed quality control. Z.Y., T.L., X.W. and C.Q. prepared data files and figures. All authors participated in the creation of the dataset, and revised the manuscript and online supporting information.

COMPETING INTERESTS

The authors declare no competing interests.

ADDITIONAL INFORMATION

Supplementary information The online version contains supplementary material available at https://doi.org/10.1038/s41612-023-00555-4.

Correspondence and requests for materials should be addressed to Guoqiang Li, Yougui Song, Kathryn E. Fitzsimmons, Shuangwen Yi, Shugang Kang, Chongyi E, Thomas Stevens, Zhongping Lai, Aditi K. Dave, Chunzhu Chen, Yanqing Deng, He Yang or Fahu Chen.